Радиофизика и радиоастрономия, 2000, т. 5, №1, стр. 84-94

УДК 533.9.01

Microwave Reflectometry in Fusion Devices

D. L. Grekov

Institute of Plasma Physics,
National Science Center "Kharkov Institute of Physics and Technology",
61108, Kharkov, Ukraine
E-mail: grekov@ipp.kharkov.ua

The paper was received July, 15, 1999

The features of microwave plasma diagnostics in fusion devices are studied. For this purpose a complete description of electromagnetic fields involved in the microwave reflectometry is made. The diagnostics features are examined for normal and oblique probing of plasma in large tokamak with non-circular cross-section. The new possibility of probing by extraordinary wave is proposed for efficient controlling the plasma density.

1. Introduction

Electron density profile measurements are among the most important tasks of plasma diagnostics. Thomson scattering and multichord submillimeter interferometry are widely used in large tokamaks for this purposes. These methods are mutually complementary. The first one allows local density measurements at certain time moments. The second one is used to measure the electron density continuously. Information on the density profile can be obtained in this case by solving the inverse problem.

The analysis of situation for ITER (International Thermonuclear Experimental Fusion Reactor) has shown [1] that the employment of the multichord interferometry meets great difficulties due to the blanket presence and the magnetic configuration with a divertor. The other method, namely, a single-chord multi frequency reflectometry, was recognized to be promising [2,3]. It was suggested and widely used as early as in the sixties. Its advantages for determining electron density profiles have been demonstrated on JET (Joint European Torus) [4].

This paper is devoted to the prospects of microwave reflectometry for fusion devices of ITER size. The analysis presented may be applied for any tokamak with sufficiently strong confining magnetic field i. e. on condition that the electron cyclotron frequency is greater or equal to the electron plasma frequency at plasma minor cross-section. The presentation is organized in the following way. Chapter 2 gives the main parameters of the ITER-scale plasma and magnetic configuration, probing frequency values and spatial dependences. Chapter 3 is concerned with the description of probing signal fields in the antenna. In addition the influence of a low density scrape-off layer plasma on the distribution of antenna-emitted fields is studied. A brief description of ray tracing technique which is used to investigate the propagation of probing signal in bulk plasma is also given here. The features of microwave probing in the equatorial plane of fusion devices are discussed in Part 4.1. In Part 4.2 a new way of quick plasma diagnosing by means of extraordinary wave is offered. The possibility of using the extraordinary wave for determining of poloidal dependence plasma density is considered in Part 4.3. The results are summarized in Conclusion.

2. Basic Principles

In a magnetized plasma, two waves may propagate transversely to the magnetic field in the electron cyclotron frequency band. The ordinary (*o*-) wave (***E*** ∥ ***B***) reflects at the point, where the condition $\omega = \omega_{pe}(r)$ is satisfied (here ω is the wave frequency, $\omega_{pe}(r) = \left(4\pi n_e e^2 / m_e\right)^{1/2}$ is the electron plasma frequency, $n_e(r)$ is the electron density). The extraordinary (*x*-) wave (***E***⊥***B***) reflects at the points, where

$$\omega = \omega_{eu} = \left(\omega_p^2 + \omega_c^2/4\right)^{1/2} + \omega_c/2\,, \qquad (1)$$

$$\omega = \omega_{el} = \left(\omega_p^2 + \omega_c^2/4\right)^{1/2} - \omega_c/2\,,$$

here ω_{eu}, ω_{el} are the upper and lower cut-off frequencies of *x*-wave, respectively (here $\omega_c = eB/m_e c$ is the electron cyclotron frequency). The reflection of *o*-wave is commonly used in electron density profile measurements. Since the position of *x*-wave cut-off points depends on both the plasma density and magnetic field value, the simultaneous probing with *o*- and *x*-waves may, in principle, enable one to determine plasma density and magnetic field profiles. For typical ITER-scale parameters ($n_e(0) = n_0 = 10^{20}\,\mathrm{m}^{-3}$, the plasma torus average minor radius $a_0 = 2.15\,\mathrm{m}$,

the device major radius $R_0 = 6$ m, plasma current $I = 22$ MA) the poloidal magnetic field at plasma boundary, $B_p = 2T$, is comparable to the toroidal magnetic field at the outer side of the plasma torus, $B_t = 3.4T$, and strongly effects the wave propagation (toroidal magnetic field at the inner side of the plasma torus equals $7.6T$).

The magnetic configuration is involved in calculations in following way. In the cylindrical system of coordinates (R,φ,Z) related to the main axis of the torus, the poloidal magnetic flux $\Psi(R,Z)$ is computed by means of EQUS code [5] based on the integral method of solution of the equilibrium equation. Then we assume that the quasi toroidal (r,ϑ,φ) and cylindrical coordinate systems are related as:

$$R = R_0 - \Delta(r) + r\cos\vartheta - \delta(r)\sin^2\vartheta,$$

$$Z = r\lambda(r)\sin\vartheta .$$

Here r is the minor radius of magnetic surface, ϑ and φ are the angles along the minor and major azimuth, respectively ($\vartheta = 0$ at the outer side of the torus), $\Delta(r)$ is the shift of magnetic surface center from R_0, $\delta(r)$ and $\lambda(r)$ are the magnetic surface ellipticity and triangularity, accordingly. The functions $\Delta(r)$, $\delta(r)$, $\lambda(r)$ are calculated numerically. Taking into account three moments provides an adequate description of device magnetic configuration apart from the vicinity of divertor

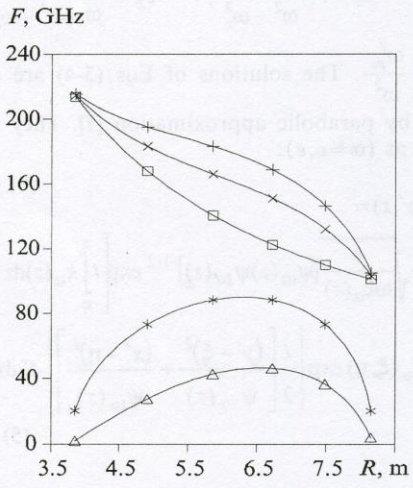

Fig. 1. *Space dependences of the lower (Δ) and upper (+) x-wave cut-off frequencies, the o-wave (*) cut-off frequency, the cyclotron frequency ($\square$), and the upper hybrid resonance frequency ($\times$) at the equatorial plane of torus*

which is inaccessible for microwave diagnostics. So we have the equations of magnetic surfaces $\Psi(r) = \text{const}$. The density was assigned as $n_e = n_e(\Psi)$, the poloidal field is determined by the poloidal flux, and the toroidal field $B_t = B_0 R_0 / R$.

The band for ITER-scale reflectometry in equatorial plane was found from the calculation of cut-off point location with the bulk plasma density profile of the form $n_e(r/a_0) = (n_0 - n_b)\left(1 - r^2/a_0^2\right) + n_b$. As shown in Fig. 1, reflection of both *o*- and *x*-waves (upper cut-off) takes place in non-overlapping bands (30÷90 GHz for the *o*-wave and 110÷220 GHz for the *x*-wave). For typical ITER parameters the *o*-wave cut-off frequency significantly differs from ω_c and the frequency ω_{cu} differs from $2\omega_c$. So the cyclotron damping of probing signals is negligibly low.

3. Microwave Beam Propagation in Fusion Devices

As shown in [1], it is possible to arrange microwave antennas in one or two poloidal cross-sections of the torus at the outward first wall. In doing so a number of antennas can be shifted away from the torus equatorial plane. However, the employment of such antennas in large D-shaped tokamak is related to a number of problems. They include the difficulty of the proper choice of probing beam angle at different frequencies and the significant decrease of probing beam intensity due to beam spreading and reflection by convex surfaces. To clarify these questions the complete 3-D model of microwave propagation is developed. The microwave frequencies and polarization are chosen so as to correspond *o*- and *x*-mode reflectometry in the ITER-scale device. First, we carry out the consecutive calculation of electromagnetic fields in antenna. Then, in low density plasma scrape-off layer (SOL) we make use of the parabolic approximation method, and finally trace the 3-D rays in a bulk plasma.

3.1. Transmitting (Receiving) Antenna

We consider the antenna as a rectangular pyramidal horn with the distance from the vortex to horn aperture $R_h = 0.25$ m; $a_h = 0.02$ m along the *X*-axis (in toroidal direction) and $b_h = 0.05$ m along the *Y*-axis (in poloidal direction). This horn acts as a transmitting and receiving antenna simultaneously. It is attached to rectangular wave guide with the side along the *X*-axis $a_g = 8\times10^{-3}$ m and the side along the *Y*-axis $b_g = 0.02$ m.

The TE_{mn}-mode field in the wave guide is

$$E_x = E_0 \cos\left[m\pi\left(\frac{x}{a_g}+\frac{1}{2}\right)\right]\times$$

$$\times\sin\left[n\pi\left(\frac{y}{b_g}+\frac{1}{2}\right)\right]\exp(ik_z z),$$

where

$$k_z = \left[k^2 - \left(\frac{m\pi}{a_g}\right)^2 - \left(\frac{n\pi}{b_g}\right)^2\right]^{1/2} \quad \text{and} \quad k = \omega/c.$$

The amplitude E_0 is chosen so that the power flux of TE_{01}-mode across the wave guide equals 1 W. We introduce the spherical coordinate system $(r_h, \vartheta_h, \varphi_h)$ centered on the top of the horn. Then neglecting the wave reflected from the horn aperture and taking into account that the horn walls practically coincide with the $\vartheta_h = \text{const}$ and $\varphi_h = \text{const}$ planes we have for the horn field:

$$E_\varphi = \frac{A}{\sqrt{kr_h}}\cos\left(\frac{\pi m\varphi_h}{\varphi_0}\right)\frac{\partial}{\partial\vartheta_h}\left[L_\upsilon^\mu(\cos\vartheta_h)\right]H_{\upsilon+1/2}^{(2)}(kr_h). \tag{2}$$

Here $H_{\upsilon+1/2}^{(2)}$ is Hankel function, L_υ^μ is the linear combination of Legendre functions, $\mu = \pi m/\varphi_0$, $\varphi_0 = \text{arctg}\left(\frac{a_h}{R_h}\right)$, $\upsilon = \frac{\pi n}{\alpha_0} - \frac{1}{2}$, $\alpha_0 = \text{arctg}\left(\frac{b_h}{R_h}\right)$, $\vartheta_h = \pi/2 - \text{arctg}(y/R_h)$. We study the propagation of the fundamental mode, m=0, n=1. In this work it is sufficient to use the zero-order approximation in matching the horn and wave guide fields. The reflection coefficient at wave guide – horn link appears to be negligibly small. The wavelength dependence of reflection coefficient K_R on the horn aperture R_h was calculated numerically. Thought the reflected signal is small, $K_R \cong 3\cdot10^{-3} \div 2\cdot10^{-2}$, it can still exceed the signal reflected from a plasma.

3.2. The Scrape-Off Layer Plasma

Let us assume that in SOL of thickness $L_s \approx 0.2$ m the plasma density varies from $n_{eh} = 10^{17}$ m^{-3} near the horn to $n_{eb} = 5\cdot10^{18}$ m^{-3} at the boundary of a bulk plasma. The magnetic field in this layer is supposed to be constant and directed at the angle β $\left(\beta = \text{arctg}\left(B_{pol}/B_t\right)\right)$ to the shorter side of a horn. The magnetic field shear may lead to a conversion of o- and x-waves. This effect develops [6] at

$$8\frac{N_o^2 + N_e^2}{\left(N_o^2 - N_e^2\right)^2}\delta_s^2 \approx 1,$$

where N_o, N_e are the refractive indices of o- and x-waves, $\delta_s = \frac{\beta c}{z_s\omega}$, z_s being the space scale of the shear. Then the effect of the shear is essential at $n_e \le 2.5\cdot10^{16}$ m^{-3} which is lower than n_{eh}. To determine the phase fronts and the probing signal amplitude distribution at a boundary of bulk plasma we shall analyze the field distribution in SOL. Let us introduce the Cartesian coordinate system (X', Y', Z) so that $0Z \| \nabla n_e$, $0X' \| \boldsymbol{B}$. For o-wave we have $E_{x'} >> E_{y'}, E_z$, for x-wave $E_{y'} >> E_z >> E_{x'}$. Since in SOL $\frac{\partial E_i}{\partial z} >> \frac{\partial E_i}{\partial x'}, \frac{\partial E_i}{\partial y'}$, Maxwell equations yield for the o-wave $(E_{x'} \equiv E_o)$:

$$\frac{\partial^2 E_o}{\partial z^2} + \frac{\omega^2}{c^2}\varepsilon_3 E_o + \frac{\partial^2 E_o}{\partial y'^2} + \varepsilon_3\frac{\partial^2 E_o}{\partial x'^2} = 0, \tag{3}$$

and for the x-wave $\left(E_{y'} \equiv E_e\right)$:

$$\frac{\partial^2 E_e}{\partial z^2} + \frac{\omega^2}{c^2}\frac{\varepsilon_1^2 - \varepsilon_2^2}{\varepsilon_1}E_e + \frac{\partial^2 E_e}{\partial y'^2} + \left(1 + \frac{\varepsilon_2^2}{\varepsilon_1^2}\right)\frac{\partial^2 E_e}{\partial x'^2} = 0, \tag{4}$$

where $\varepsilon_1 = 1 - \frac{\omega_{pe}^2}{\omega^2 - \omega_c^2}$, $\varepsilon_2 = \frac{\omega_c}{\omega}\frac{\omega_{pe}^2}{(\omega^2 - \omega_c^2)}$, $\varepsilon_3 = 1 - \frac{\omega_{pe}^2}{\omega^2}$. The solutions of Eqs. (3-4) are obtained by parabolic approximation [7]. They are written as $(\alpha = o, e)$:

$$E_\alpha(x', y', z) =$$

$$= -\frac{iA_\alpha}{2\pi}\sqrt{\frac{c}{\omega k_\alpha(z)}}\left[\psi_{1\alpha}(z)\psi_{2\alpha}(z)\right]^{-1/2}\exp\left[i\int_0^z k_\alpha(z)\mathrm{d}z\right]\times$$

$$\times\int_{-\infty}^{\infty}\int E_\alpha(\xi,\eta)\exp\left\{\frac{i}{2}\left[\frac{(y'-\xi)^2}{\psi_{2\alpha}(z)} + \frac{(x'-\eta)^2}{\psi_{1\alpha}(z)}\right]\right\}\mathrm{d}\xi\mathrm{d}\eta. \tag{5}$$

Here

$$k_o(z) = \frac{\omega}{c}\varepsilon_3^{1/2}(z), \quad k_e(z) = \frac{\omega}{c}\left[\frac{\varepsilon_1^2(z) - \varepsilon_2^2(z)}{\varepsilon_1(z)}\right]^{1/2},$$

$$\psi_{1o}(z)=\frac{c^2}{\omega^2}\int_0^z k_o(z')\mathrm{d}z',\ \psi_{2o}(z)=\int_0^z \mathrm{d}z'/k_o(z'),$$

$$\psi_{1e}(z)=\int_0^z \frac{\varepsilon_1^2(z')+\varepsilon_2^2(z')}{\varepsilon_1^2(z')}\frac{\mathrm{d}z'}{k_e(z')},$$

$$\psi_{2e}(z)=\int_0^z \frac{\mathrm{d}z'}{k_e(z')},\ E_o(\xi,\eta)=E_\varphi(\xi,\eta)\cos\beta,$$

$E_e(\xi,\eta)=E_\varphi(\xi,\eta)\sin\beta$, $E_\varphi(\xi,\eta)$ is given by Eq. (2). At $\beta=0$ or $n_e=0$ the integrals (5) can be calculated analytically. They are expressed in terms of Fresnel function. At large distances, $z>>a_h b_h\omega/c$, the expressions (5) turn to known expressions for the far-zone field of antenna. For vacuum we have $\psi_{1\alpha}(z)=\psi_{2\alpha}(z)=z\,c/\omega$, i. e. $z=\omega\psi_{1,2\alpha}/c$. The effect of plasma can be characterized by the shift of z, viz, for the X'-axis z changes to $z_\parallel=\omega\psi_{1\alpha}(z)/c$, and for the Y'-axis z transforms into $z_\perp=\omega\psi_{2\alpha}(z)/c$. As shown in Fig. 2 the low density plasma has no effect on x-wave field distribution in SOL. But for the o-wave in long wavelength band the SOL effect is noticeable. The level lines of o-wave amplitude at bulk plasma boundary are plotted in Fig. 3. They are not symmetrical in poloidal direction. This deviation is caused by low density plasma. The probing signal amplitude distributions in SOL were calculated for the o-wave and x-wave. We have put the density profile to be $n_e=n_{e0}(z/L_s)^2$. The density profile variation weakly influences field distribution in SOL. As can be seen in Fig. 4, x-wave amplitude $(\lambda=2\ \mathrm{mm})$ does not decrease as $1/z$. This confirms the inapplicability of far-zone approximation for description of the field distribution at bulk plasma boundary. These calculations make possible to construct starting wave fronts at bulk plasma boundary as well as to determine the probing signal amplitude distribution at this fronts, and initial wave vectors.

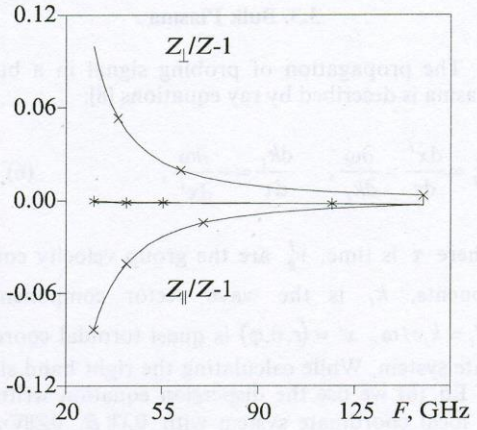

Fig. 2. *Frequency dependences of the parameters $z_\perp/z$, $z_\parallel/z$ for the o-wave (×) and x-wave (*). If plasma affects the field distributions the parameters differ from unity*

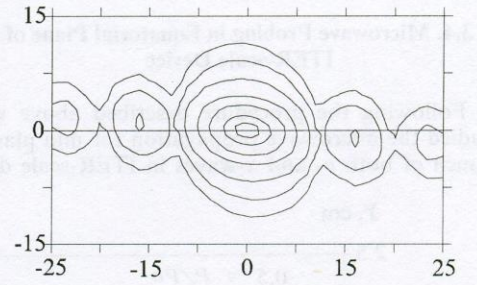

Fig. 3. *O-wave amplitude level lines at bulk plasma boundary (the abscissa and ordinate axes correspond to toroidal and poloidal directions, respectively)*

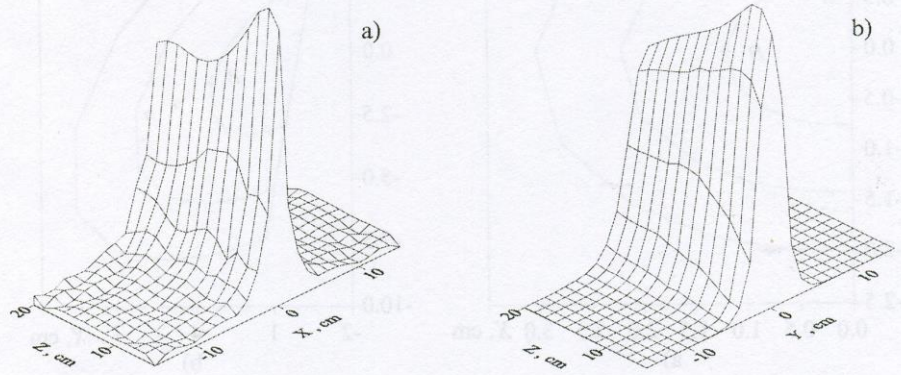

Fig. 4. *The amplitude of x-wave probing signal with F=150 GHz in the scrape-off layer. Z-axis corresponds to radial direction. (a) X-axis corresponds to toroidal direction and (b) Y-axis corresponds to poloidal direction*

3.3. Bulk Plasma

The propagation of probing signal in a bulk plasma is described by ray equations [8]:

$$v_g^i = \frac{dx^i}{d\tau} = \frac{\partial \omega}{\partial k_i}, \quad \frac{dk_i}{d\tau} = -\frac{\partial \omega}{\partial x^i}, \qquad (6)$$

where τ is time, v_g^i are the group velocity components, k_i is the wave vector components, $N_i = k_i c/\omega$, $x^i = (r, \vartheta, \varphi)$ is quasi toroidal coordinate system. While calculating the right hand side of Eq. (6) we use the dispersion equation written in local coordinate system with $0X \| \boldsymbol{B}$, $0Z \| \nabla n_e$, $N_\| = \boldsymbol{NB}/B$, $N_\perp = \left(N^2 - N_\|^2\right)^{1/2}$ as:

$$\varepsilon_1 N_\perp^4 + \left[(\varepsilon_1 + \varepsilon_3)\left(N_\|^2 - \varepsilon_1\right) + \varepsilon_2^2\right] N_\perp^2 + \varepsilon_3\left[\left(N_\|^2 - \varepsilon_1\right)^2 - \varepsilon_2^2\right] = 0.$$

Both the total phase shift and the ray transition time are calculated.

3.4. Microwave Probing in Equatorial Plane of ITER-scale Device

Following the procedure described above we studied the microwave propagation for mid plane launch of both *o*- and *x*-waves in ITER-scale device and estimated the power reflected back to receiving antenna. For this purpose we determined the region S_i at bulk plasma boundary in front of the transmitting antenna where the probing signal power decreases by 10 % . Further on, we call this region the "starting spot". Then we calculated the wave vector components at the boundary of starting spot (typically, at 11 points), the amplitude A_i at the spot center and the spot area S_i. Using the ray tracing we found the area of a spot S_f reflected to the torus outside. The attenuation of a signal that has come to the receiving antenna is given by $\gamma = \frac{A_i^2 S_i}{\iint_{S_h} A_h^2 ds} \frac{S_h}{S_f}$, where S_h is the horn area, A_h is the probing signal amplitude in the horn aperture. We note once again that the transmitting antenna is simultaneously a receiving one. The starting and reflected spots of *o*-wave are shown in Fig. 5. One can see that the reflected spot expands and undergoes some deformation. The projections of the rays started at the point A onto poloidal and toroidal torus cross sections are shown in Fig. 6. Note that the rays started at point A (or B) have a zero wave vector component in toroidal (poloidal) direction. Nevertheless, the rays show a displacement in these directions. This effect, first indicated in [9], is due to the action of poloidal magnetic field. However, for the point B

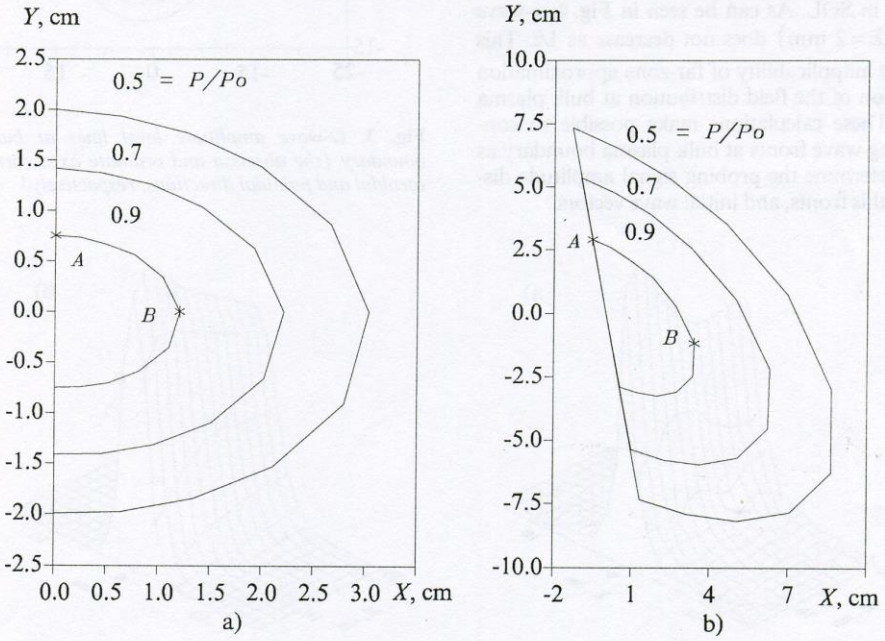

Fig. 5. *Starting (a) and reflected (b) spots of the o-wave probing signal with F=43 GHz, P/P_0 is the ratio of signal power at a level line to that at the spot center. The figures (a) and (b) have different scales*

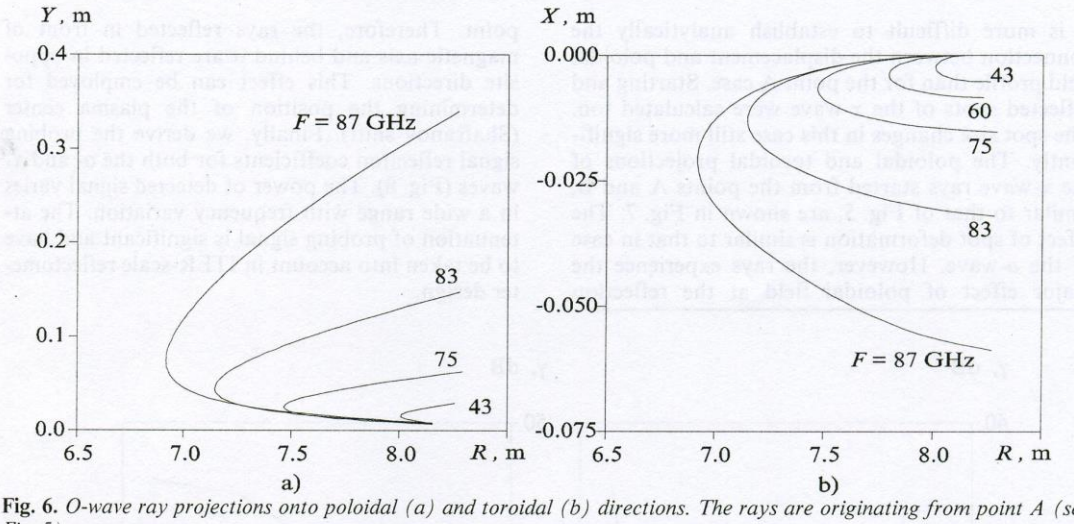

Fig. 6. *O-wave ray projections onto poloidal (a) and toroidal (b) directions. The rays are originating from point A (see Fig. 5)*

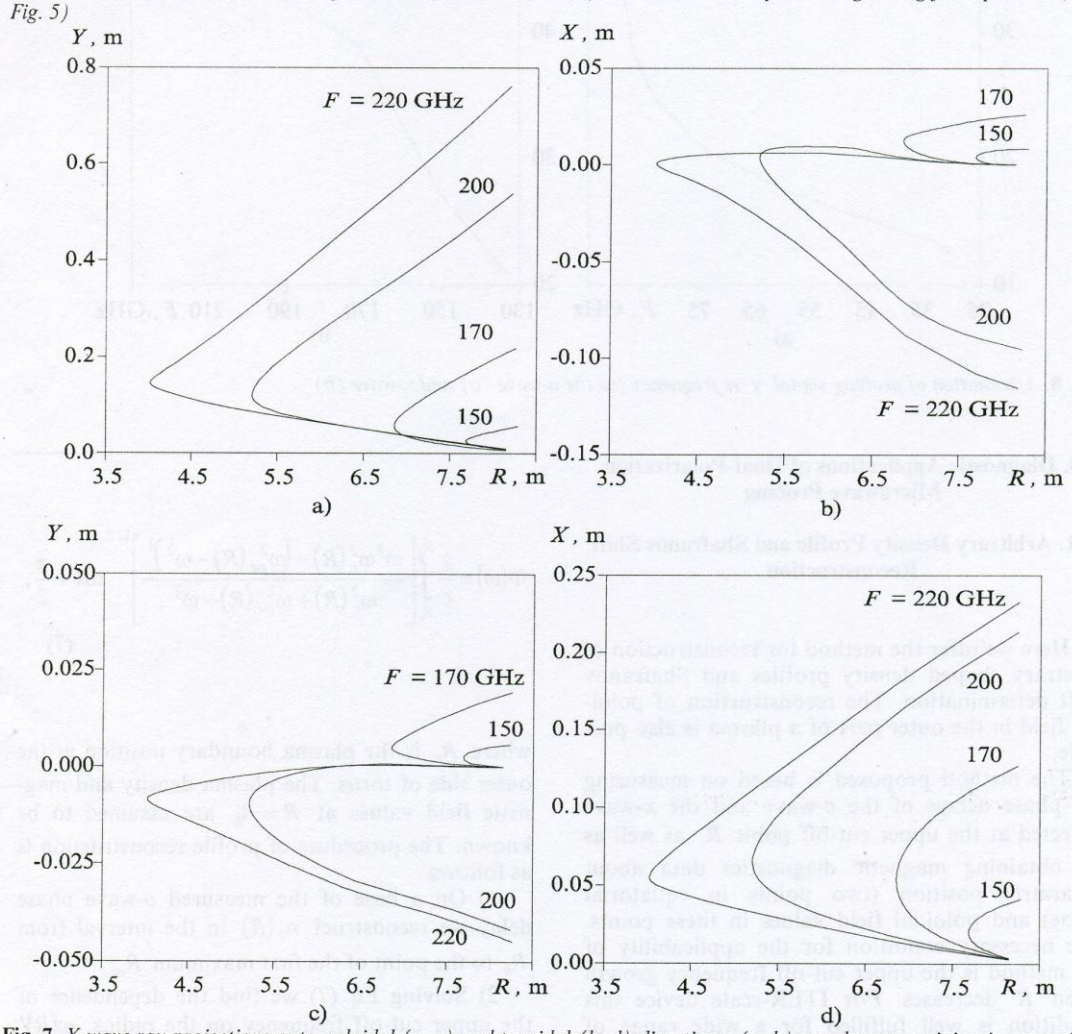

Fig. 7. *X-wave ray projections onto poloidal (a, c) and toroidal (b, d) directions. (a, b) are the rays originating at point A, (c, d) are the ones from point B (similar to Fig. 5)*

it is more difficult to establish analytically the connection between the displacement and poloidal field profile than for the point A case. Starting and reflected spots of the x-wave were calculated too. The spot size changes in this case still more significantly. The poloidal and toroidal projections of the x-wave rays started from the points A and B, similar to that of Fig. 5, are shown in Fig. 7. The effect of spot deformation is similar to that in case of the o-wave. However, the rays experience the major effect of poloidal field at the reflection point. Therefore, the rays reflected in front of magnetic axis and behind it are reflected in opposite directions. This effect can be employed for determining the position of the plasma center (Shafranov shift). Finally, we derive the probing signal reflection coefficients for both the o- and x-waves (Fig. 8). The power of detected signal varies in a wide range with frequency variation. The attenuation of probing signal is significant and have to be taken into account in ITER-scale reflectometer design.

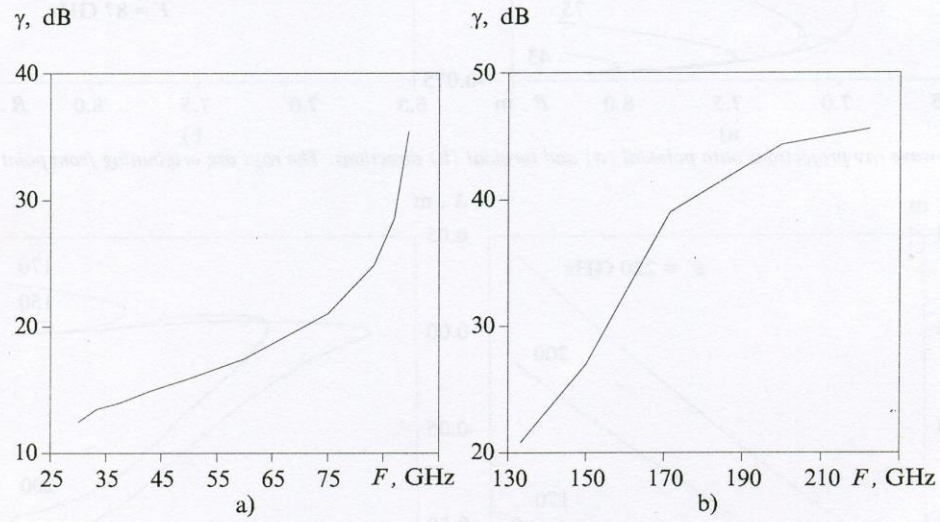

Fig. 8. *Attenuation of probing signal* γ *vs frequency for the o-wave (a) and x-wave (b)*

4. Diagnostic Applications of Dual-Polarization Microwave Probing

4.1. Arbitrary Density Profile and Shafranov Shift Reconstruction

Here we offer the method for reconstruction of arbitrary shaped density profiles and Shafranov shift determination. The reconstruction of poloidal field in the outer part of a plasma is also possible.

The method proposed is based on measuring the phase delays of the o-wave and the x-wave reflected at the upper cut-off point R_c as well as on obtaining magnetic diagnostics data about separatrix position (two points in equatorial plane) and poloidal field values in these points. The necessary condition for the applicability of the method is the upper cut-off frequency growth when R decreases. For ITER-scale device this condition is well fulfilled for a wide range of plasma density values (Fig. 1). The x-wave phase delay is given by

$$\Phi(\omega)=\frac{2}{c}\int_{R_c}^{R_b}\left[\frac{\omega^2\omega_c^2(R)-\left(\omega_{pe}^2(R)-\omega^2\right)^2}{\omega_c^2(R)+\omega_{pe}^2(R)-\omega^2}\right]^{1/2}\mathrm{d}R+\frac{\pi}{2}, \tag{7}$$

where R_b is the plasma boundary position at the outer side of torus. The plasma density and magnetic field values at $R=R_b$ are assumed to be known. The procedure of profile reconstruction is as follows.

1) On a base of the measured o-wave phase delay we reconstruct $n_e(R)$ in the interval from R_b to the point of the first maximum R_m.

2) Solving Eq. (7) we find the dependence of the upper cut-off frequency on the radius, $\omega(R)$, and $\omega_c(R)$ at $R_b \div R_m$ region.

3) We assume that magnetic axis is shifted from R_0 by a distance $\Delta(0)=\Delta_0$ and magnetic surfaces are shifted by $\Delta(r)=\Delta_0\dfrac{\exp(\zeta)-\exp\left(\zeta r^2/a_0^2\right)}{\exp(\zeta)-1}$, where ζ is the free parameter. It is supposed that at $(R_0+\Delta_0, R_m)$ region the poloidal field $B_p(r)$ changes linearly from 0 to the value $B_p(R_m)$ determined from Eq. (7). This assumption is reasonable because the region considered lies in the plasma interior where $B_p \ll B_t$.

4) Solving Eq. (7) and using the results of x-wave phase delay measurements we find $\omega(R)$ and $n_e(R)$ at $(R_0+\Delta_0, R_m)$. The original algorithm [10] created to solve Eq. (7) was applied in 2)-4). As compared to already known algorithms, it allows us to get $R(\omega)$ more accurately.

5) Regarding the plasma density to be constant on magnetic surfaces we extend $n_e(R)$ to the interval between $R_0+\Delta_0$ and torus inner boundary. Then we use the data of x-wave phase delay for the frequency band where cut-off points are at the inner part of plasma column.

Using these, we minimize the functional:

$$\Psi(\Delta_0,\zeta)=\sum_k\left[\Phi(\omega_k)-\Phi_s(\omega_k,\Delta_0,\zeta)\right]^2 \qquad (8)$$

over the parameters Δ_0 and ζ. Here Φ is the measured phase delay and Φ_s is that reconstructed with use of assigned Δ_0, ζ, $n_e(R)$. The most reliable way of finding the minimum of $\Psi(\Delta_0,\zeta)$ is based on using the magnetic diagnostics data. These allows us to connect the parameters ζ and Δ_0 through the B_{pout}/B_{pin}:

$$\Delta_0=-\frac{B_{pout}R_{out}-B_{pin}R_{in}}{B_{pout}R_{out}+B_{pin}R_{in}}\frac{a_0}{2\zeta}(1-\exp(-\zeta)).$$

Then the functional (8) has a pronounced minimum over Δ_0. The reconstructed profiles of arbitrary prescribed plasma density and poloidal magnetic field in ITER-scale device are shown in Fig. 9. We studied the stability of this method with respect to errors of phase delay measurements. The results are rather optimistic and confirm the reliability of the information about plasma density profile, Shafranov shift, and outer part of poloidal field profile within an acceptable errors level.

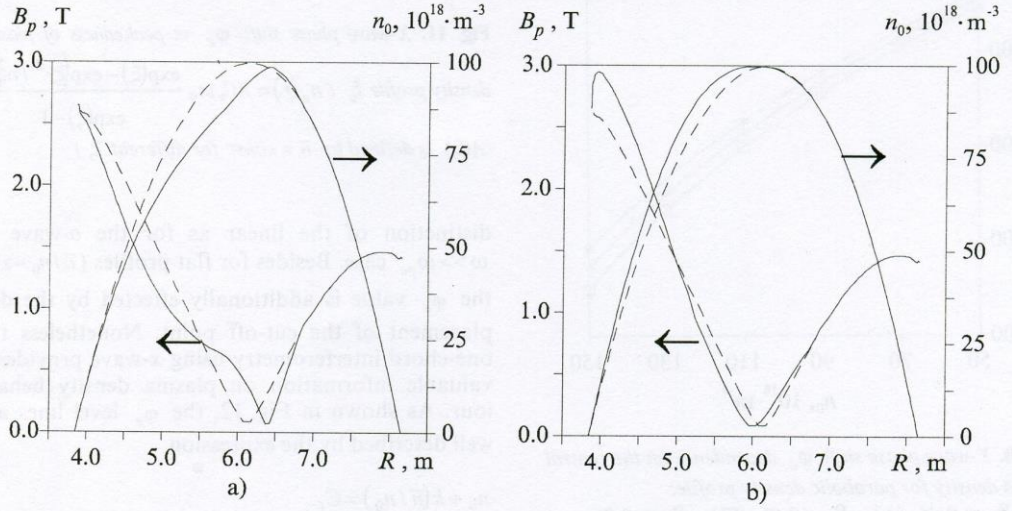

Fig. 9. *Reconstructed profiles of plasma density and poloidal magnetic field in ITER (the magnetic configuration at the 90 s of discharge). Dashed lines – prescribed profiles, solid lines – found profiles. The first and second steps of iterations are shown. At final step prescribed profiles and found profiles are practically the same*

4.2. The X-Wave Interferometry

To date the single-chord interferometry using the o-wave with the frequency $\omega \gg \omega_{pe}$ is one of the most widely used operative means to get information on so-called linear averaged density:

$$n_L = L\bar{n} = \int_0^L n_e(s)\,ds,$$

with L being the ray path. This diagnostics is used on both small and large devices. Its application for operative diagnostics in fusion devices is compli-

cated by the difficulties of arranging the diagnostic equipment on torus inner side.

In view of this we propose to use x-wave midplane launch for obtaining operative information on plasma density. As Fig. 1 shows, when passing from outer to inner side of minor cross-section ω_{eu} increases monotonously and at the inner edge of a plasma $\omega_{eu} = \omega_{is}$ weakly depends on plasma density. So, by choosing $\omega \approx \omega_{is}$ and measuring the phase delay of the beam reflected in the equatorial plane:

$$\varphi_e = 2\int_{-a_0}^{a_0} k_z \mathrm{d}r ,$$

we get information on plasma density. As it is seen from Fig. 10, the dependence of φ_e on the density peak value n_0 is well defined and for the parabolic density profile gives an insignificant error in calculating n_0 with β_p ($\beta_p = 4\pi(\overline{n_i T_i + n_e T_e}) / B_p^2(a_0)$,

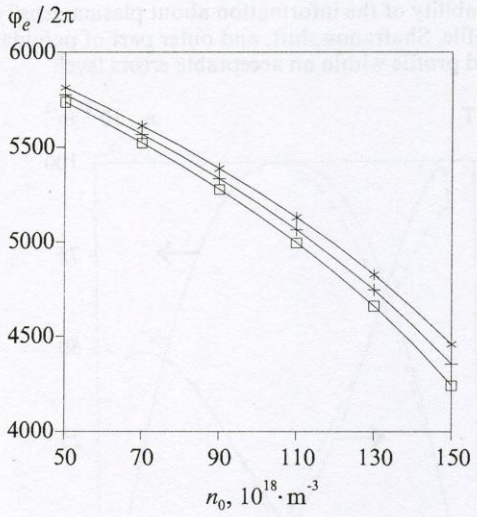

Fig. 10. *X-wave phase shift* φ_e *dependence on the central plasma density for parabolic density profile:* (*) – $\beta_p = 0.46$, (+) – $\beta_p = 0.61$, (□) – $\beta_p = 0.76$

where n_i is the ion density, T_i, T_e the ion and electron temperatures, respectively) varying in a wide range. What kind of density data can be obtained on using the x- wave? The plasma density can be characterized by its peak value n_0 and the rate of profile peakedness $\overline{n}/n_0$. Returning to one-chord interferometry we note that it cannot give information about these both parameters. Therefore, it should be use such a generalized parameter as $\overline{n} = n_0(\overline{n}/n_0)$. For the x-wave the phase delay at $\overline{n} = \text{const}$ strongly depends on the $\overline{n}/n_0$ ratio, i. e., on the plasma density profile (Fig. 11) because $n_e(r)$ enters the expression for $k_z(r)$ in a rather complicated way in

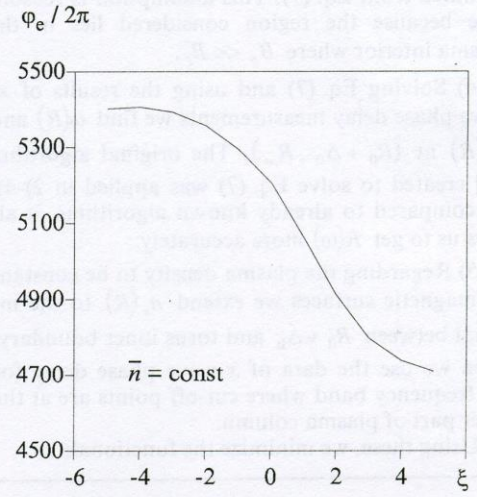

Fig. 11. *X-wave phase shift* φ_e *vs peakedness of plasma density profile* ξ ($n_e(r) = A(\xi) n_0 \dfrac{\exp(\xi) - \exp\left(\xi r^2 / a_0^2\right)}{\exp(\xi) - 1}$, $A(\xi)$ *is defined by* $\overline{n} = const$ *for different* ξ)

distinction of the linear as for the o-wave in $\omega >> \omega_{pe}$ case. Besides for flat profiles ($\overline{n}/n_0 \to 1$), the φ_e value is additionally effected by the displacement of the cut-off point. Nonetheless the one-chord interferometry using x-wave provides a valuable information on plasma density behaviour. As shown in Fig. 12, the φ_e level lines are well described by the expression

$$n_0 + k(\overline{n}/n_0) = C_i .$$

Here C_i is constant. Its value depends on measured phase shift. The k-factor depends on operating conditions and configuration of particular device. So, the method proposed enables us to determine the sum of n_0 and $\overline{n}/n_0$. It can be used for operative control of plasma density behavior. Simultaneous use of diagnostics presented and traditional one-chord interferometry would provide operative information on the peak density value and profile peakedness.

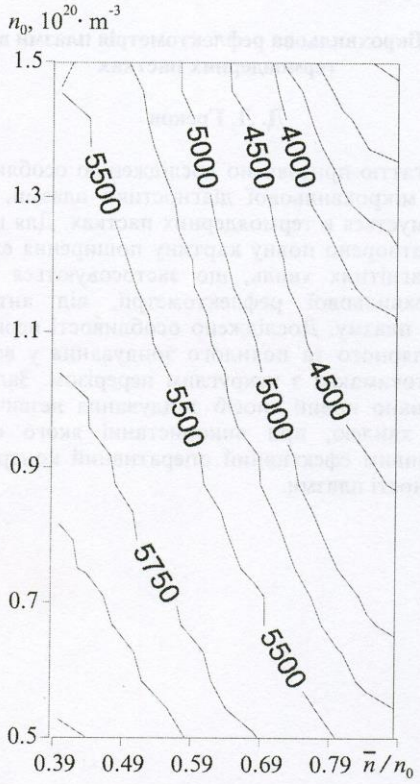

Fig. 12. $\varphi_e = const$ *lines at* $n_0 - \bar{n}/n_0$ *plane*

4.3. The X-wave Tomography

The fusion devices design allows us to accommodate reflectometry antenna not only in torus equatorial plane. An additional antenna for transmitting and receiving probing signals can be installed in poloidal cross section on torus outer side. In this case the employment of *x*-wave seems to be the most promising. The probing signal frequency should be chosen in upper cut-off frequency band so that the signals would reflect from the surface close to the plasma boundary at the torus inner side. Then the position of reflecting surface changes a little with variations in the peak density and plasma density profile. A special choice of antenna tilt angles ensures the reception of probing signal from each transmitting antenna by two receiving antennas. The probing rays cover a significant part of minor cross-section. Practically, the rays are straight lines. The phase delay data along these lines may serve the basis for determining poloidal dependence of the plasma density.

5. Conclusions

The possibilities and prospects of applying the reflectometry for fusion plasma diagnostics are presented. The comprehensive analysis of *o*- and *x*-mode microwave propagation for midplane and off-midplane outward launch has shown that the microwaves launched from the realistic antenna at a midplane of tokamak are reflected backwards to transmitting antenna. The reflected signal is strongly attenuated due to finite beam divergence and long distance from antenna to reflecting layers. It is shown that midplane dual-polarization reflectometry can be effectively used for electron density and poloidal magnetic field reconstruction. For specific conditions of ITER-scale plasma $(\omega_{pe}(0) \sim \omega_c(0))$ the *x*-mode outward launch allows to measure the *x*-mode cut-off layer position along the whole plasma diameter. For such situation the reconstruction of $n_e(R)$- and $B(R)$-profiles looks feasible even if *o*-mode inward launch will be impractical. We also have shown that the *x*-mode reflectometry channel with the frequency chosen to reflect at the inward plasma edge ($F \sim 220$ GHz) can be used for monitoring the average electron density whereas the *x*-mode off-midplane launch with properly oriented antennas can be used for taking an additional information on poloidal dependence of a fusion plasma density.

Acknowledgments

Author is grateful to Prof. O. S. Pavlichenko for many valuable discussions.

References

1. ITER Diagnostics. ITER Documentation Series, No. 33. Vienna, IAEA, 1990, 58 pp.
2. G. Vayakis, T. Ando, N. Bretz et al. Diagnostics for Experemental Thermonuclear Fusion Reactors 2. New York, Plenum Press, 1998, pp. 97-106.
3. V. Vershkov, M. Manso, G. Vayakis et al. Diagnostics for Experemental Thermonuclear Fusion Reactors 2. New York, Plenum Press, 1998, pp. 107-118.
4. R. Prentice, P. Cripwell, A.E. Costley et al. Proc. 15th Europ. Conf. Contr. Fusion and Plasma Heating (Dubrovnik,1988). Vienna, IAEA, 1988, **12B**, Part 3, pp. 1115-1118.
5. L. E. Zakharov. J. Tech. Phys. 1974, **44**, No. 8, pp. 1608-1613.
6. V. V. Zheleznyakov, V. V. Kocharovsky, Vl. V. Kocharovsky. J. Exp. Theor. Phys. 1979, **77**, No. 1, pp. 101-113.
7. V. A. Fock. Electromagnetic Diffraction and Propagation Problems. New York, Pergamon Press, 1965, 320 pp.
8. W. R. Hamilton. Mathematical Papers 1931, 1, Geometrical Optics, Cambridge University Press.

9. D. L. Grekov, O. S. Pavlichenko. J. Tech. Phys. Lett. 1990, **16,** No. 22, pp. 34-37.
10. A. V. Bomko, D. L. Grekov, O. S. Pavlichenko. J. Tech. Phys. Lett. 1992, **18,** No. 19, pp. 6-10.

Микроволновая рефлектометрия плазмы в термоядерных ловушках

Д. Л. Греков

Статья посвящена исследованию особенностей микроволновой диагностики плазмы в термоядерных ловушках. Для этого построена полная картина прохождения от антенны в плазму электромагнитных полей, применяемых для микроволновой рефлектометрии. Исследованы особенности перпендикулярного и наклонного зондирования в больших токамаках с некруглым сечением. Предложен новый способ зондирования необыкновенной волной, при использовании которого возможен эффективный оперативный контроль плотности плазмы.

Мікрохвильова рефлектометрія плазми в термоядерних пастках

Д. Л. Греков

Статтю присвячено дослідженню особливостей мікрохвильової діагностики плазми, що утримується в термоядерних пастках. Для цього відтворено повну картину поширення електромагнітних хвиль, що застосовуються для мікрохвильової рефлектометрії, від антени крізь плазму. Досліджено особливості перпендикулярного та похилого зондування у великих токамаках з некруглим перерізом. Запропоновано новий спосіб зондування незвичайною хвилею, при використанні якого стає можливим ефективний оперативний контроль щільності плазми.